*Original Article*

# Impulsive energy conversion with magnetically coupled nonlinear energy harvesting systems

**Quanqi Dai, Inhyuk Park and Ryan L Harne**(iD)

## Abstract
Magnets have received broad attention for vibration energy harvesting due to noncontact, nonlinear forces that may be leveraged among harvesting system elements. Yet, opportunities to integrate multi-directional coupling among a nonlinear energy harvesting system subjected to impulsive excitations have not been scrutinized, despite widespread prevalence of such excitations. To characterize these potentials, this research investigates an energy harvesting system with magnetically induced nonlinearities and coupling effects under impulsive excitations. A system model is formulated and validated with experimental efforts to reconstruct static and dynamic properties of the system via simulations. Then, the model is harnessed to scrutinize dynamic response of the system when subjected to impulse conditions. This research reveals the clear impulse strength dependence and influence of asymmetries on total electrical energy capture and energy conversion efficiency that are tailored by magnetic force coupling. Asymmetry is found to promote greater impulse-to-electrical energy conversion when compared to the symmetric counterpart system and a benchmark nonlinear energy harvester. The roles of initial conditions exemplify how stored energy in an asymmetric energy harvesting system may be released during nonlinear impulsive response. These results provide insights about opportunities and challenges to incorporate magnetic coupling effects in nonlinear energy harvesting systems subjected to impulses.

## Keywords
Energy harvesting, magnetic forces, impulsive vibration

## Introduction

Proliferating microelectronic devices with low electrical power needs have stimulated demands for self-sufficient powering solutions, especially by kinetic energy harvesting (Randall, 2011; Shenck and Paradiso, 2001). Propelled by practical aspects of vibration energy harvesting, researchers have investigated fundamental methods of designing and deploying energy harvesters subjected to diverse kinetic energy sources (Erturk, 2011; Scruggs and Jacob, 2009; Seuaciuc-Osório and Daqaq, 2010). Among ambient excitation forms, impulsive excitations are widespread in natural and engineered environments (Shenck and Paradiso, 2001; Stacoff et al., 2005; Ylli et al., 2015). Researchers have studied the dynamic response of linear energy harvesters subjected to direct mechanical impacts (Gu and Livermore, 2011; Umeda et al., 1996) and noncontact magnetic force impulses (Kulah and Najafi, 2008; Pillatsch et al., 2012). Alternatively, stiffness nonlinearities, especially bistability (Erturk and Inman, 2011; Harne and Wang, 2017; Panyam et al., 2014), have

been investigated to cultivate large amplitude dynamics, ideal for kinetic energy capture, due to triggering snap-through behaviors in arbitrary excitation environments (Harne and Wang, 2014; Masana and Daqaq, 2011; Tang et al., 2010). The alternating current (AC) power generation from single bistable energy harvesters resulting from impulsive excitations has been closely characterized and shown to be sensitive to initial conditions (Harne et al., 2016; Wickenheiser and Garcia, 2010). Exploiting bistable nonlinearities for energy harvesting from impulsive excitations is thus widely considered as an opportune means to capture kinetic energies from many operational environments (Jung and Yun, 2010; Suhaimi et al., 2014).

Department of Mechanical and Aerospace Engineering, The Ohio State University, Columbus, OH, USA

**Corresponding author:**
Ryan L Harne, Department of Mechanical and Aerospace Engineering, The Ohio State University, Columbus, OH 43210, USA.
Email: harne.3@osu.edu

Magnetic forces have played notable roles in such investigations due to highly adjustable means to transfer impulsive energies without harmful, physical contact to the harvesters (Kulah and Najafi, 2008; Pillatsch et al., 2012) and also due to abilities to introduce nonlinearities including bistability (Harne et al., 2016; Wickenheiser and Garcia, 2010). The versatility of such magnetic forces extends to effecting system dynamics in multiple dimensions despite uniaxial input. Using two magnetically coupled bistable beams, Andò et al. (2013) investigated a bi-directional nonlinear energy harvester, while Su and Zu (2013, 2014) studied bi- and tri-directional energy harvesters using similar magnetically coupled structures. Yang and Towfighian (2017a, 2017b) demonstrated that internal resonance and variable potential energy functions may be effective approaches to improve energy harvesting efficiency and broaden frequency bandwidth of magnetically coupled nonlinear energy harvesters. In addition, the interaction of magnetic forces has also been investigated for use in magnetoelectric generators for both broadband frequency and multi-directional energy harvesting capabilities (Lin et al., 2016; Yang et al., 2013). Considering the breadth of investigations, magnetic forces have been considered to transmit single impulses, to introduce nonlinearities, or to realize coupling within vibration energy harvesting systems. Yet, there is still a lack of knowledge on strategies that integrate these principles to leverage magnetic forces for impulse transmission among multiple nonlinear energy harvesters. This knowledge gap prevents researchers from capitalizing on magnetic coupling influences in vibration energy harvesting systems that may be favorably deployed in the myriad operating environments where impulsive energies exist.

To shed light on these unknowns, this research investigates the electrodynamic responses of impulsively excited vibration energy harvesters with magnetically induced nonlinearity and magnetic coupling effects. The direct current (DC) power delivery is examined due to the meaningful nonlinearities introduced by such practical rectification circuitry (Guyomar et al., 2005; Roundy et al., 2003). The following sections first introduce the platform and model of the energy harvesting system considered here. Then, comparisons between numerical and experimental results are used to validate the model. Detailed investigations are then undertaken to quantify the influences of asymmetries on the resulting DC power generation in such magnetically coupled platforms. These dynamic responses are contrasted to a benchmark case previously studied in the literature to quantify the electrical enhancement provided by the system composition and coupling. The major new findings are summarized in the last section.

# An exemplary energy harvester system with magnetically induced nonlinearity and coupling

Magnetoelastic structures have multiple advantages for energy harvesting applications, including the capability to incorporate a wide range of nonlinear characteristics (Feeny and Yuan, 2001; Hikihara and Kawagoshi, 1996; Moon and Holmes, 1979; Schaeffer and Ruzzene, 2015) and to couple dynamic responses without direct elastic interfacing elements (Andò et al., 2013; Kulah and Najafi, 2008; Pillatsch et al., 2012; Su and Zu, 2013, 2014). One effective use of magnetic forces to tune nonlinearities is to use a pair of repulsive magnets such that a magnet, fixed to a reference frame, is positioned along the centerline of a movable magnet attached to the free tip of a cantilevered energy harvester beam (Erturk et al., 2009). Similar principles have been used to couple multiple cantilevers (Andò et al., 2013; Su and Zu, 2013). Building from such understanding of opportunities via magnetic force interactions, in this research two nonlinear piezoelectric cantilevers are studied, which use repulsive magnet pairs to introduce nonlinearities and tailor beam coupling.

Figure 1(a) shows a photograph of the experimental setup. Each harvester beam is formed by a piezoelectric cantilever (Midé Technology) clamped in an aluminum mount with an aluminum magnet holder and a neodymium magnet at the cantilever tip. The magnets attached to the ends of the cantilevers are hereby termed "magnet 1" and "magnet 2" as shown in Figure 1(b). A magnet fixed to the reference frame is also incorporated, termed "magnet 3," to induce a broad range of nonlinearities. Based on the magnetic polarizations indicated in Figure 1(b), the force between magnets 1 and 2 at the tips of the cantilevers is repulsive. The fixed magnet 3 also creates repulsive force with respect to magnet 2 on the cantilevered harvester beam 2 tip, while magnet 3 and magnet 1 on the cantilevered harvester beam 1 free tip result in attractive forces. For AC–DC voltage conversion, diode bridge rectifiers and smoothing circuits are connected to the outputs of the piezoelectric beams. For brevity of notation hereafter, the two piezoelectric energy harvesting cantilevers are termed "beam 1" and "beam 2" in accordance with labels in Figure 1(b).

# Modeling of the magnetically coupled nonlinear energy harvester system

A model is formed of the energy harvesting system shown in Figure 1 to provide more effective insight than that obtained through exhaustive number of experiments that may involve small uncertainties in the undertaking. The model presumes that each cantilever
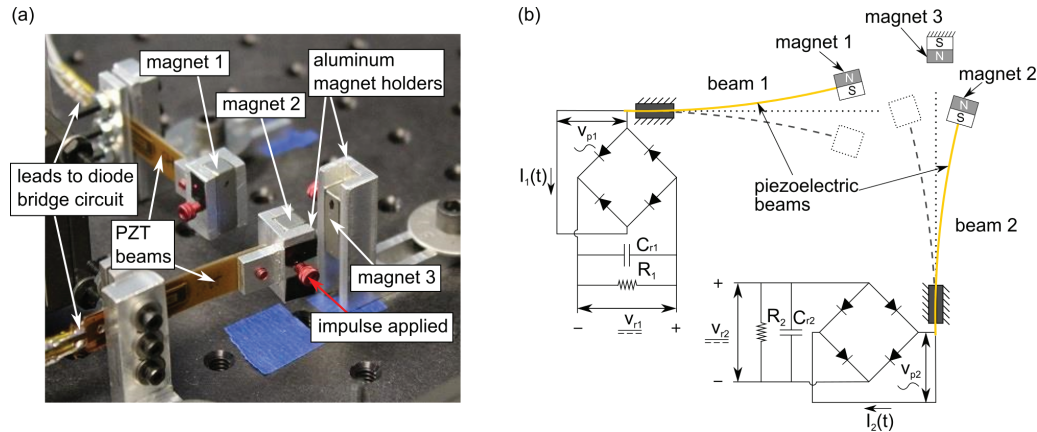
(a)



(b)

**Figure 1.** (a) Photograph of experimental energy harvester composition and location where impulses are applied. (b) Top view schematics of energy harvester platform and rectifier circuits.

oscillates in its lowest order vibration mode, to reduce the partial differential equations of motion to the equation respecting only the lowest order generalized displacement (Erturk and Inman, 2009). Thus, using Newton's and Kirchhoff's laws the governing equations of motion for the magnetically coupled nonlinear energy harvester system are derived

$$m_1\ddot{x}_1 + c_1\dot{x}_1 + k_{11}x_1 + k_{31}x_1^3 + \alpha_1 v_{p1} = F_{21} + F_{31} \quad (1a)$$

$$m_2\ddot{x}_2 + c_2\dot{x}_2 + k_{12}x_2 + k_{32}x_2^3 + \alpha_2 v_{p2} = F_{32} + F_{12} \quad (1b)$$

$$C_{pi}\dot{v}_{pi} + I_i = \alpha_i\dot{x}_i \; (i = 1, 2) \quad (1c)$$

In equation (1), $x_1$ and $x_2$ denote the lowest order generalized translational displacements of the two cantilevers termed beam 1 and beam 2, respectively; $m_i$ ($i = 1, 2$) denote the equivalent mass of each cantilever in addition to the respective tip mass; $c_i$, $k_{1i}$, and $k_{3i}$ ($i = 1, 2$) are, respectively, the viscous damping, linear stiffness, and nonlinear stiffness of beam 1 and 2, using conventional large deflection theory to yield the nonlinear stiffness terms (Hodges, 1984); the electromechanical coupling effects for two beams are quantified by parameters $\alpha_i$ ($i = 1, 2$); the AC voltages from two piezoelectric beams are represented by $v_{pi}$ ($i = 1, 2$); the internal capacitances of the piezoelectric beams are $C_{pi}$ ($i = 1, 2$); and the overdot operator represents differentiation with respect to time $t$.

The rectifiers are assumed to be perfect. Therefore, the AC from the piezoelectric beams is denoted by $I_i(t)$ ($i = 1, 2$) and related to the AC voltages $v_{pi}$ and DC voltages $v_{ri}$ ($i = 1, 2$) by (Shu and Lien, 2006)

$$I_i(t) = \begin{cases} C_{ri}\dot{v}_{ri} + \frac{v_{ri}}{R_i}, & \text{if } v_{pi} = v_{ri} \\ -C_{ri}\dot{v}_{ri} - \frac{v_{ri}}{R_i}, & \text{if } v_{pi} = -v_{ri} \; (i = 1, 2) \\ 0, & \text{if } |v_{pi}| < v_{ri} \end{cases} \quad (2)$$

Here, $C_{ri}$ and $R_i$ ($i = 1, 2$) are the smoothing capacitors and load resistances, respectively, used for each rectifier

circuit shown in Figure 1(b). The piezoelectric harvester beams in the experimental setup are bimorphs and are composed of sequential polyimide and steel shim layers. Each polyimide layer contains a portion of PZT-5H and a circuit lead. A central polysulfone layer prevents shorting between the PZT of the adjacent unimorphs from one half of the beam thickness to the other. Despite the seven layers of material for each beam, the total mass of each beam, including the circuit tabs shown at the bottom left of Figure 1(a), is around 1 g. Correspondingly, the aluminum magnet holder and neodymium magnet held at each cantilever beam tip have a total mass of around 5.6 g. As a result, the mass ratio between the total tip mass and the cantilever beam is relatively large, so that rotation of the beam tips is not negligible. The rotational motion is especially important because it governs the magnetic forces. Thus, in the model the rotations of the beam tips are taken into account, as shown in Figure 2. The rotations of the tips of beams 1 and 2, respectively, generate angles $\theta_1$ and $\theta_2$. In addition, as shown in Figure 2, the imperfection in the alignment of magnet 3 is also considered by a small angle $\theta_3$ deviation away from the reference coordinate system.

To account for the rotation of the piezoelectric cantilever tips, the transverse vibration of each cantilever $w_i(x, t)$ is characterized by the lowest order motion

$$w_i(x, t) = x_i(t)\phi_i(x) \quad (3)$$

where $x_i$ and $\phi_i$ denote the lowest order generalized displacement and normal mode for each cantilever beam, and $i = 1, 2$ is the index for beams 1 and 2.

The lowest order normal mode for each cantilever is

$$\phi_i(x) = C_{1,i}\cos\beta_{1,i}x + C_{2,i}\sin\beta_{1,i}x + C_{3,i}\cosh\beta_{1,i}x$$
$$+ C_{4,i}\sinh\beta_{1,i}x$$

$$(4)$$

where $C_{1,i}$, $C_{2,i}$, $C_{3,i}$, and $C_{4,i}$ $(i = 1, 2)$ are four constants that may be reduced to relations to just one constant using the clamped-free boundary conditions. Thus, the lowest order normal mode for each cantilever is expressed as

$$\phi_i(x) = C_4\left[(\sin\beta_{1,i}x - \sinh\beta_{1,i}x) - \frac{\sin\beta_{1,i}l_i + \sinh\beta_{1,i}l_i}{\cos\beta_{1,i}l_i + \cosh\beta_{1,i}l_i}(\cos\beta_{1,i}x - \cosh\beta_{1,i}x)\right] \qquad (5)$$

The lowest order normal mode is normalized such that the modal displacement at the cantilever tip is unity (Zhang et al., 2017). Consequently, given that the cantilever beam lengths are $l_i$ $(i = 1, 2)$, the constant parameter $C_4$ is

$$C_4 = \frac{1}{\left[(\sin\beta_{1,i}l_i - \sinh\beta_{1,i}l_i) - \frac{\sin\beta_{1,i}l_i + \sinh\beta_{1,i}l_i}{\cos\beta_{1,i}l_i + \cosh\beta_{1,i}l_i}(\cos\beta_{1,i}l_i - \cosh\beta_{1,i}l_i)\right]} \quad (i = 1, 2) \qquad (6)$$

In equations (4) to (6), $\beta_{1,i}$ $(i = 1, 2)$ is the first eigenvalue determined from the frequency equation

$$1 + \frac{1}{\cos\beta_{n,i}l_i\cosh\beta_{n,i}l_i} - R_i\beta_{n,i}l_i(\tan\beta_{n,i}l_i - \tanh\beta_{n,i}l_i)$$
$$= 0 \; (i = 1, 2) \qquad (7)$$

where $R_i = (m_{ti}/\rho_i A_i l_i)$ $(i = 1, 2)$ denotes the mass ratio of each cantilever beam; $m_{ti}$ $(i = 1, 2)$ is the cantilever tip mass that is the mass of the aluminum magnet holder and neodymium magnet; and $\rho_i$ and $A_i$ $(i = 1, 2)$ are the density and cross-sectional area of each cantilever beam.

As the piezoelectric beams oscillate, magnets 1 and 2 rotate by

$$\theta_i = w_i'(l_i, t) = \frac{(\cos\beta_{1,i}l_i - \cosh\beta_{1,i}l_i) - \frac{\sin\beta_{1,i}l_i + \sinh\beta_{1,i}l_i}{\cos\beta_{1,i}l_i + \cosh\beta_{1,i}l_i}(-\sin\beta_{1,i}l_i - \sinh\beta_{1,i}l_i)}{(\sin\beta_{1,i}l_i - \sinh\beta_{1,i}l_i) - \frac{\sin\beta_{1,i}l_i + \sinh\beta_{1,i}l_i}{\cos\beta_{1,i}l_i + \cosh\beta_{1,i}l_i}(\cos\beta_{1,i}l_i - \cosh\beta_{1,i}l_i)}\beta_{1,i}x_i(t) \; (i = 1, 2) \qquad (8)$$

With the knowledge of the beam tip rotations, using the notation of Figure 2, the total displacements of the harvester beam tips from undeflected positions are

$$d_i = x_i + a\sin(\theta_i) \; (i = 1, 2) \qquad (9)$$

where $a$ denotes half of the side length of the square magnets.

After defining the rotations of magnets 1 and 2, the magnetic forces are determined. $F_{mn}$ in equation (1) denote the magnetic force acting on magnet $n$ due to the effects of magnet $m$ along the transverse direction of either $\hat{i}$ or $\hat{j}$ as indicated in Figure 2. Based on a dipole–dipole model (Stanton et al., 2010; Yung et al., 1998), the magnetic forces are

$$F_{21} = \frac{3\mu_0 M_1 V_1 M_2 V_2}{4\pi} \frac{5r_{12,\hat{j}}A_{1,21} + A_{2,21}\left(r_{12,\hat{i}}^2 + r_{12,\hat{j}}^2\right)}{\left(r_{12,\hat{i}}^2 + r_{12,\hat{j}}^2\right)^{7/2}} \qquad (10a)$$

$$F_{31} = \frac{3\mu_0 M_1 V_1 M_3 V_3}{4\pi} \frac{-5r_{13,\hat{j}}A_{1,31} + A_{2,31}\left(r_{13,\hat{i}}^2 + r_{13,\hat{j}}^2\right)}{\left(r_{13,\hat{i}}^2 + r_{13,\hat{j}}^2\right)^{7/2}} \qquad (10b)$$

$$F_{12} = \frac{3\mu_0 M_1 V_1 M_2 V_2}{4\pi} \frac{-5r_{12,\hat{i}}A_{1,21} + A_{3,21}\left(r_{12,\hat{i}}^2 + r_{12,\hat{j}}^2\right)}{\left(r_{12,\hat{i}}^2 + r_{12,\hat{j}}^2\right)^{7/2}} \qquad (10c)$$

$$F_{32} = \frac{3\mu_0 M_2 V_2 M_3 V_3}{4\pi} \frac{-5r_{23,\hat{i}}A_{1,32} + A_{3,32}\left(r_{23,\hat{i}}^2 + r_{23,\hat{j}}^2\right)}{\left(r_{23,\hat{i}}^2 + r_{23,\hat{j}}^2\right)^{7/2}} \qquad (10d)$$

where

$$A_{1,mn} = (r_{nm,\hat{i}}\cos\theta_n + r_{nm,\hat{j}}\sin\theta_n)(r_{nm,\hat{i}}\cos\theta_m + r_{nm,\hat{j}}\sin\theta_m) \qquad (11a)$$

$$A_{2,mn} = r_{nm,\hat{i}}\sin(\theta_n + \theta_m) + 2r_{nm,\hat{j}}(\sin\theta_n\sin\theta_m + \cos(\theta_n - \theta_m)) \qquad (11b)$$

$$A_{3,mn} = 2r_{nm,\hat{i}}(\cos\theta_n\cos\theta_m + \cos(\theta_n - \theta_m)) + r_{nm,\hat{j}}\sin(\theta_n + \theta_m) \qquad (11c)$$

In equation (9), $\mu_0$ is the permeability constant $4\pi \times 10^{-7} \, \text{N/A}^2$; $M_n$ and $V_n$ $(n = 1, 2, 3)$ represent the magnetization and magnet volume of each magnet, which collectively determine the magnetic moment values $\mu_n = M_n V_n$ $(n = 1, 2, 3)$ as shown in Figure 2; $r_{nm,\hat{i}}$ and $r_{nm,\hat{j}}$ are the components of the position vectors in the $\hat{i}$ and $\hat{j}$ directions, respectively, for magnet $n$ with
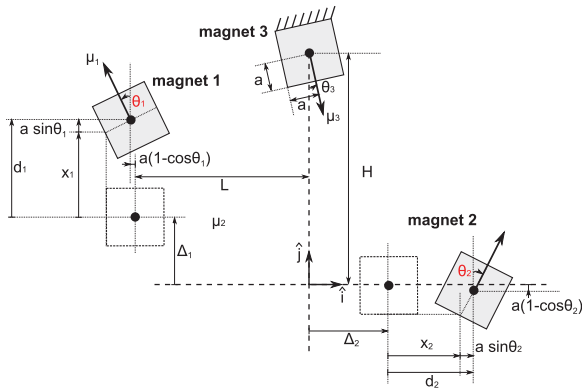
**Figure 2.** Detailed schematics of the coordinate system, spacing parameters, and magnetic moment vectors. The deflected and rotated positions of the magnets are shown by shaded squares, while the undeflected positions of magnets 1 and 2 are indicated by hollow dashed squares.

respect to magnet $m$. Based on the schematic shown in Figure 2, the position vectors are

$$\vec{r}_{12} = r_{12,i}\hat{i} + r_{12,j}\hat{j} = -(L + d_2 + \Delta_2 + a(1 - \cos\theta_1))\hat{i} \\ + (d_1 + \Delta_1 + a(1 - \cos\theta_2))\hat{j}$$

(12a)

$$\vec{r}_{13} = r_{13,i}\hat{i} + r_{13,j}\hat{j} = -(L + a(1 - \cos\theta_1))\hat{i} \\ - (H - d_1 - \Delta_1)\hat{j}$$

(12b)

$$\vec{r}_{21} = r_{21,i}\hat{i} + r_{21,j}\hat{j} = (L + d_2 + \Delta_2 + a(1 - \cos\theta_1))\hat{i} \\ - (d_1 + \Delta_1 + a(1 - \cos\theta_2))\hat{j}$$

(12c)

$$\vec{r}_{23} = r_{23,i}\hat{i} + r_{23,j}\hat{j} = (d_2 + \Delta_2)\hat{i} - (H + a(1 - \cos\theta_2))\hat{j}$$

(12d)

where $L$ and $H$ denote the spacing parameters respecting the reference coordinate system; $\Delta_1$ is the center offset distance between magnets 1 and 2; and $\Delta_2$ is the center offset distance between magnets 2 and 3. These notations are shown in Figure 2.

The model presented above is suitable to determine the electrodynamic responses of the magnetically coupled nonlinear energy harvesting system induced by impulsive events. This model is utilized in subsequent sections of this work to probe the parametric

sensitivities of the system not immediately apparent via the intricate equations of motion and positional relations.

## Experimental and simulation methods

Measurements from the experimental setup shown in Figure 1(a) are acquired using the following methods. The transient electrodynamic responses induced by impulses on beam 2 are the source of the system dynamics considered in this work. The impulses are applied at the point indicated by the red arrow in Figure 1(a) using fast manual taps. Such impulses may be envisioned to originate from diverse energies such as human motion-based (Ylli et al., 2015) or transportation-based (Ansari and Karami, 2015) impulses. The beam tip displacements, corresponding to the displacements of magnets 1 and 2 at the cantilever tips, are measured by two laser displacement sensors (ILD-1420; Micro Epsilon). The harvester beam tip velocities are derived from the displacement data. The AC voltage and rectified DC voltage across load resistances are collected independently for each piezoelectric beam. All channels of data are recorded at a sampling frequency of 4096 Hz and digitally filtered by a low-pass filter below 200 Hz. The experimentally identified system parameters are shown in Table 1. The equivalent masses $m_i$ $(i = 1, 2)$ are obtained according to harvester beam properties and dimensions with respect to the assumed lowest order mode response of a cantilever. The natural frequencies (and thus linear stiffnesses $k_{1i}$ $(i = 1, 2)$) and damping constants $c_i$ $(i = 1, 2)$ are obtained by evaluating transient, free vibration responses of each beam. With the knowledge of the stable equilibrium positions in accordance with the single-degree-of-freedom response assumed for each beam, the parameters $k_{3i}$ $(i = 1, 2)$ are then computed. The properties of magnet are approximated from the manufacturer-supplied information, while the piezoelectric cantilever properties are measured directly or obtained from the manufacturer.

To validate the energy harvesting system model and to build detailed knowledge on the system characteristics, direct numerical simulations of the governing equations are undertaken using fourth-order Runge–Kutta numerical integration. Simulation results presented in the following sections use the experimental

**Table 1.** Experimentally identified system parameters ($i$ = 1, 2).

| $m_i$ (g) | $c_i$ (N s/m) | $k_{1i}$ (N/m) | $k_{3i}$ (MN/m³) | $\rho_i$ (kg/m³) | $A_i$ (mm²) | $l_i$ (mm) | $a$ (mm) |
|---|---|---|---|---|---|---|---|
| 7.0 | 0.03 | 320 | 3.28 | 3500 | 7.5 | 34 | 3.175 |

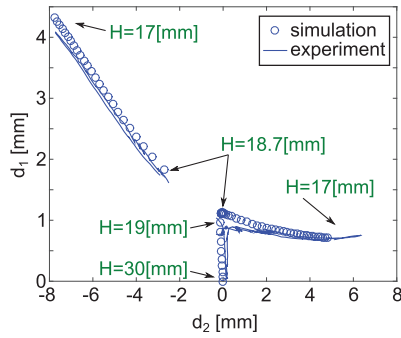| $\alpha_i$ (mN/V) | $C_{pi}$ (nF) | $C_{ri}$ (µF) | $R_i$ (kΩ) | $M_1$ (MA/m) | $M_2, M_3$ (MA/m) | $V_1, V_2, V_3$ (cm³) | |
|---|---|---|---|---|---|---|---|
| 0.2 | 5 | 2.2 | 1000 | 1.1 | 1.25 | 0.768 | |

**Figure 3.** Experimentally measured static equilibria (solid line) of magnets 1 and 2 at the cantilever tips and the corresponding simulation results (data point) when the distance $H$ is decreasing in the directions as indicated by arrows.

parameter values given in Table 1. For dynamic simulations, the impulse–momentum theorem is used to correlate a given initial energy input to a harvester beam to the corresponding initial velocity used for the transient simulations. When compared to the measurements, simulations use the initial velocities identified from the experimental data. At least 100 periods of oscillation are computed for each set of initial conditions to capture sufficient durations of nonlinear impulse responses for sake in the subsequent numerical data post-processing.

With such numerical and experimental findings, this research seeks to close the knowledge gap regarding opportunities to exploit magnetic nonlinearity and coupling effects in an impulsively excited energy harvesting system. Due to the severe nonlinearities, multi-dimensional motions, and intricate equation system that represents the full electrodynamic responses, analytical efforts are not currently considered because necessary simplifying assumptions may reduce the fidelity of the insights. Such theoretical work may be considered in future research efforts.

## Results and discussion

### Validation of static equilibria and study of potential energy profiles

To verify the modeling of the strongly nonlinear magnetic forces and moments that couple together the energy harvesting system motion, the static, stable equilibria of the piezoelectric cantilever tip magnets are first studied as functions of change in the position of magnet 3. Figure 3 demonstrates the results from experiments and simulations, generated by incremental change in the position of magnet 3 which correspondingly changes the stable equilibria of magnets 1 and 2. Note that stable equilibria of magnets 1 and 2 are denoted by the total displacement $d_i$ ($i = 1, 2$) of the harvester beam tips from the undeflected positions shown in Figure 2. The solid curves in Figure 3

represent the experimental measurements for the case that the distance $H$, between magnet 3 and magnet 2, is varied from 30 to 17 mm at a nearly quasi-static rate. Prior to this change in the distance $H$, the starting stable equilibria are set to zero, that is, $d_i = 0$ ($i = 1, 2$). The positive directions of $d_i$ ($i = 1, 2$) in Figure 3 agree with displacements of magnets 1 and 2 in the $\hat{j}$ and $\hat{i}$ axes, respectively, as shown in Figure 2.

Starting from the combination of stable equilibria given by $(d_1, d_2) = (0, 0)$, the attractive force $F_{31}$ acting on magnet 1 due to magnet 3 as $H$ decreases causes beam 1 to move toward the approaching magnet 3, while the stable equilibrium of beam 2 is relatively unaffected. Yet, once the distance between magnet 3 and magnet 2 is sufficiently small, the repulsive force $F_{32}$ overcomes the elastic restoring forces of the cantilever and deflects beam 2 from $d_2 = 0$. As such, the stable equilibrium of beam 2 may take on either positive or negative values, which evidences that beam 2 exhibits a bistable nonlinearity well known for such repulsive magnet pair in energy harvesting contexts (Stanton et al., 2010). In addition, due to the associated bifurcation between the monostable and bistable system configurations, the stable equilibria may vanish around the bifurcation point (Stanton et al., 2010). In consequence, a discontinuity exists between the separate stable equilibrium "branches" shown in Figure 3, which suggest that small asymmetries exist in the system (Virgin and Wiebe, 2013). As the distance $H$ decreases further, the stable equilibrium position in $d_1$ increases if the stable equilibrium location of beam 2 $d_2$ takes on negative values indicating that the beam 2 tip is closer to the beam 1 tip. Alternatively, if the stable equilibrium deflections of beam 2 $d_2$ take on positive values, which represent greater distances from beam 1, the stable equilibrium positions $d_1$ for beam 1 remain around the value of $+ 1$ mm.

Numerical simulations of the stable equilibria are concurrently undertaken. Data points in Figure 3 correspond to the simulation results. To account for the nuanced asymmetries and imperfectly known parameters of the experiments, the simulation results are generated considering that the distance $H$ decreases from 30 to 17 mm, while the distance $L$ slightly increases from 23 to 25 mm. In addition, offset values are included as determined experimentally, including a constant small rotation angle $\theta_3 = 2°$ on magnet 3 and displacement offsets $\Delta_1 = 1.5\,\text{mm}$, $\Delta_2 = -1.15\,\text{mm}$, where the variable notation is shown in Figure 2. Due to the strongly nonlinear magnetic forces, the small offset values are found to be critical to take into account for accuracy in the response prediction. The offset values used are identified from the experiments. The simulation results shown in Figure 3 are in good qualitative and quantitative agreement with the experimental measurements. This supporting comparison validates the accuracy of the model to accurately account for the
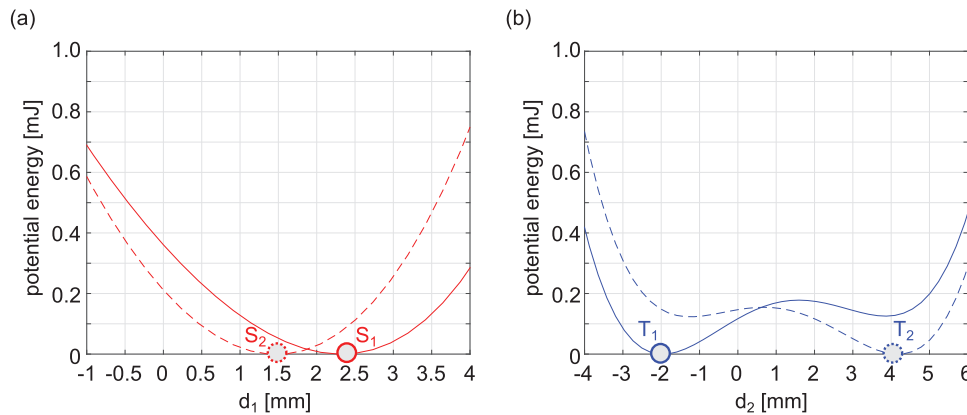
**Figure 4.** (a) Static stable equilibria ($S_1$, $S_2$) and potential energy profile of beam 1 evaluated when beam 2 is fixed at stable equilibria $T_1$ (solid) and $T_2$ (dashed); (b) static stable equilibria ($T_1$, $T_2$) and potential energy profile of beam 2 as evaluated when beam 1 is fixed at stable equilibria $S_1$ (solid) and $S_2$ (dashed).

strong nonlinearity and coupling induced by magnetic forces in the energy harvesting system.

Bistable structures may release stored energy when acted upon by impulses (Simitses, 1990). Consequently, understanding how the potential energy profiles of the cantilevers vary due to change in the position of magnet 3 is critical to understand the roles of stored and released energies when compared to input and captured energies in the vibration energy harvesting context. The validated model equations are then used to generate the potential energy profiles shown in Figure 4 using the distance parameters $L = 26$ mm and $H = 18.5$ mm, displacement offsets $\Delta_1 = 1.5$ mm and $\Delta_2 = -1.15$ mm, and alignment angle $\theta_3 = 0°$. The static equilibria of the harvester beams are indicated by filled circles in Figure 4.

For these parameters, the stable equilibria of the beam 1 tip are shown in Figure 4(a) as $d_1 = 2.323$ mm ($S_1$) and $d_1 = 1.477$ mm ($S_2$), while the stable equilibria of the beam 2 tip are shown in Figure 4(b) as $d_2 = -1.967$ mm ($T_1$) and $d_2 = 4.183$ mm ($T_2$). Clearly, these stable equilibria are the local minima of the potential energy profiles shown by curves in Figure 4. The dashed and solid curves in Figure 4(a) are, respectively, evaluated when the tip magnet for beam 2 rests at $T_2$ and $T_1$. It is evident by the constant convexity of the potential energy profiles that the harvester beam 1 is monostable regardless of the equilibria adopted by the beam 2 tip magnet. On the other hand, Figure 4(b) shows the double-well potential energy profiles of beam 2 which are evident of bistable nonlinearity. The solid and dashed curves in Figure 4(b) are evaluated when the tip magnet for beam 1 rests at positions $S_1$ and $S_2$. For these cases, the potential energy profiles of beam 2 are nearly mirror symmetric. This suggests an equivalence of dynamic response regardless of around which of the stable equilibria the beam tip magnet mass may oscillate. Yet, it is clear that a small potential energy difference exists between the two profiles of

Figure 4(b). Thus, due to impulsive excitation, beam 2 may release stored potential energy if an impulse acts on it while it rests in the local (but not global) equilibrium. As such, one may anticipate that greater electrical energy capture may result, although this energy conversion is not externally input by the impulse. This particular nuance of mechanical properties in nonlinear and magnetically coupled energy harvesters encourages the following careful quantification of energy "generated" from the impulsive excitations. As anticipated, and as studied in the latter sections of this report, by changing the distance parameters $L$ and $H$, asymmetric bistable potential energy profiles for beam 2 may be induced.

## Validation of electrodynamic, nonlinear impulse responses

To assess the accuracy of the model to predict the dynamic behaviors of the magnetically coupled nonlinear vibration energy harvesting system, transient impulse responses from experiments and simulations are compared. The amplitudes of impulses on the beam 2 tip magnet are quantified by the initial velocity amplitude. By way of experimental data acquisition, the static equilibria $S_2$ and $T_2$ are associated with zero displacement values, which is equivalent to uniform shifts of displacement $d_i$ ($i = 1, 2$) when compared to the displacement notation in simulations. Despite the uniform displacement shift, the relative displacements observed in simulation and experiment are directly comparable. Here, the distance parameters are $L = 26$ mm and $H = 18.5$ mm, displacement offsets are $\Delta_1 = 1.5$ mm and $\Delta_2 = -1.15$ mm, and the alignment angle is $\theta_3 = 0°$. Altogether, these parameters result in mirror symmetry in the beam 2 double-well potential energy profile shown in Figure 4(b).

When a small initial velocity perturbation is applied to beam 2, the transient impulse responses are presented
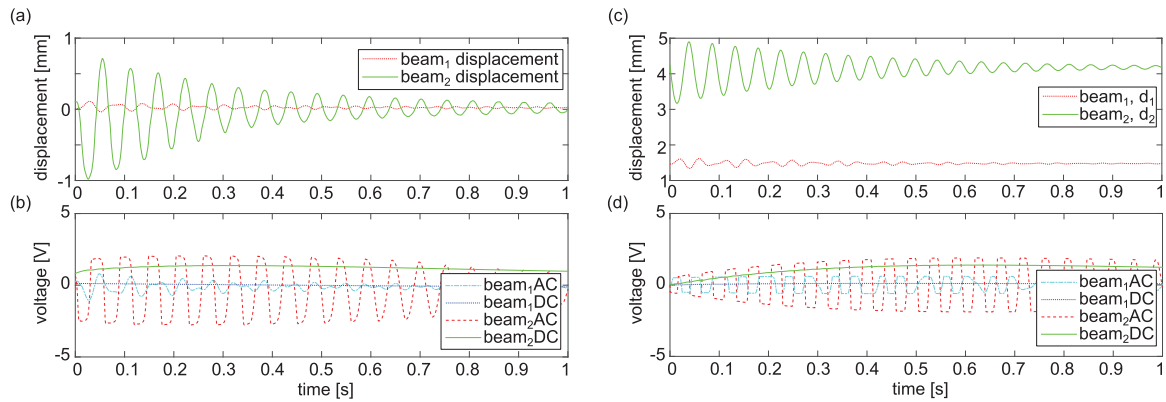
**Figure 5.** Experimental measurements of (a) harvester beam tip magnet displacements and (b) AC and DC voltages for an initial velocity on beam 2 of 0.108 m/s. (c, d) Corresponding simulation results with an initial velocity on beam 2 of 0.11 m/s.
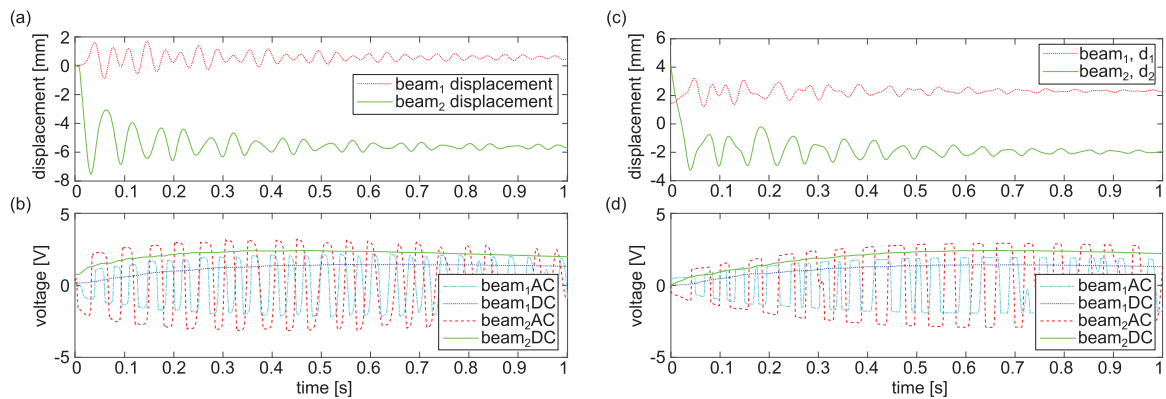


**Figure 6.** Experimental measurements of (a) harvester beam tip magnet displacements and (b) AC and DC voltages for an initial velocity on beam 2 of 0.27 m/s. (c, d) Corresponding simulation results with an initial velocity on beam 2 of 0.25 m/s.

in Figure 5. Figure 5(a) and (b) shows the experimentally measured responses of (a) beam tip displacement and (b) AC and DC voltages over a 1-s duration immediately after the impulse is applied. The small impulse is equivalent to an initial velocity of 0.108 m/s on beam 2. Beam 2 generates a small peak displacement amplitude around 1 mm and a DC voltage peak of about 1.38 V. Remnant charge stored on the smoothing capacitor $C_2$ explains the nonzero DC voltage at the initial time. Comparatively, beam 1 is nearly motionless with insignificant voltage generation. Simulation results with 0.11 m/s initial velocity on beam 2 as shown in Figure 5(c) and (d) demonstrate comparable trends as experiments. Imperfect knowledge of initial experimental conditions encourages small deviation of the initial velocity to obtain comparable trends. These results as shown in Figure 5 are intuitive because, when the beam 1 and 2 tip magnets oscillate around the stable equilibria $S_2$ and $T_2$ with small amplitude oscillations, the distance between the tip magnets 1 and 2 is large. As such, the magnetic forces generated between them are small and a small amount of the

impulse into beam 2 will be transmitted to beam 1. Overall, these small amplitude transient responses demonstrate a good agreement between experiments and simulations for validation purposes.

The small amplitude motions in Figure 5 are of less importance in the context of capturing and converting impulsive kinetic energy to electrical power. Figure 6(a) and (b) then shows the measured transient responses induced when the initial velocity amplitude on beam 2 is increased to 0.27 m/s. The initial stable equilibria are $S_2$ and $T_2$. It can be seen from Figure 6(a) that this greater impulse causes a transition from one stable equilibrium to the other for beam 2 such that it comes to rest and oscillates around the stable equilibrium closer to magnet 1. In this situation, the tip magnet on beam 1 is acted upon by the greater magnetic coupling forces and causes greater electrodynamic oscillations. These coupled behaviors result in greater DC voltage outputs of around 1.46 and 2.42 V from beams 1 and 2, respectively, as shown in Figure 6(b). The simulation results in Figure 6(c) and (d) are in good agreement with the qualitative and quantitative trends of the experiments.
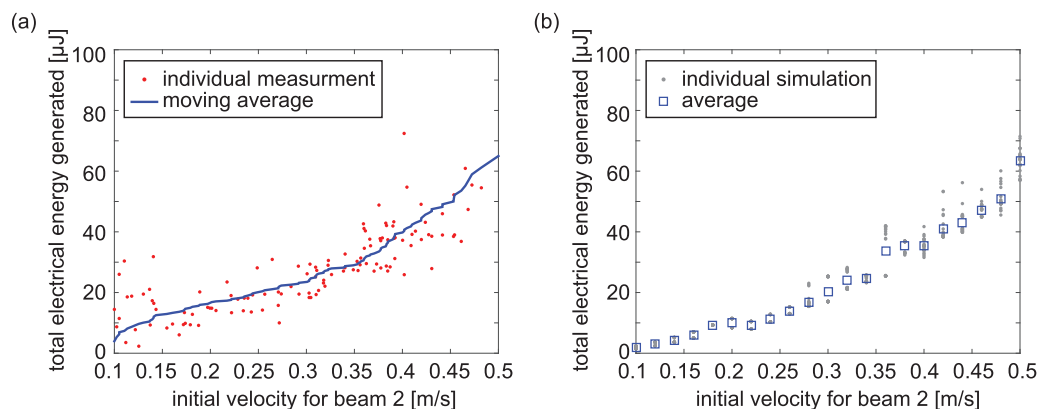
**Figure 7.** (a) Experimental measurements of total electrical energy generation (dots) and the moving average (solid curve) for different initial velocities on beam 2. (b) Corresponding simulation results evaluated at discrete initial velocities.

The more nonlinear oscillations shown in Figure 6 reveal clear interactions between the two magnetoelastic harvester beams. The oscillations shown in Figure 5 for the smaller impulse input are mostly linear and weakly coupled, while the electrodynamic oscillations in Figure 6 provide evidence for strong coupling forces between magnets 1 and 2 for impulse transmission and greater electrical energy conversion.

Based on the transient responses examined in Figures 5 and 6, the magnetically coupled nonlinear energy harvesting system cultivates a wide range of DC voltage output as a function of impulse strength, in proportion to the initial velocity on beam 2. Figure 7 provides a more comprehensive assessment of the influence of initial velocity. Figure 7(a) shows the experimental results of total electrical energy generation as a function of the initial velocity on beam 2. Each data point in Figure 7(a) is a single measurement of the integration of instantaneous DC power for 1.5 s after the impulse is applied, which is sufficient for the transient electromechanical responses to diminish to negligible values. All stable equilibrium combinations for beams 1 and 2 are considered in the experiments according to the near-mirror-symmetric double-well potential energy profile of beam 2. The solid curve in Figure 7(a) is the moving average of the individual measurements. Based on energy conservation principles, it is intuitive that the total electrical energy increases with a parabolic trend as the initial velocity on beam 2 increases. Figure 7(b) shows the corresponding simulation results obtained by 24 evaluations at each initial velocity using random initial conditions of displacement normally distributed around the stable equilibria. In Figure 7(b), each dot corresponds to an individual simulation result computed by integrating instantaneous DC power over 100 periods after impulses are applied, while the squares are the mean total energy values. The 100-oscillation period time duration is similarly chosen to be sufficient to allow transient behaviors to decay. The random

variations of initial displacement explain the deviations of the total electrical energy generated in a given simulation. A similar parabolic relationship between the initial velocity on beam 2 and the total electrical energy generated is observed in the simulation results as that observed experimentally.

These results validate the model in its accurate characterization of the nonlinear dynamic coupling influences present between the piezoelectric cantilevers of the energy harvesting system. Yet, the results in Figure 7 are also not surprising based on conservation of energy principles and do not shed special light on the roles of the magnetic coupling in the nonlinear energy harvesting system toward promoting enhanced electrical energy conversion. Indeed, as exemplified through the results of the following section, it is the tuning of configurational asymmetry in the harvesting system that gives rise to more energetic dynamic behaviors better suited for energy harvesting than the more symmetrically configured system investigated in this section.

## Examinations of the magnetically coupled nonlinear energy harvesting system with asymmetry

Moving beyond the special case when the harvester beam 2 has a near-mirror-symmetric double-well potential energy profile, this section scrutinizes the roles of asymmetric double-well potential energy profiles of beam 2 on the resulting electrical energy capture. Here, the validated model and simulation approach are leveraged to characterize the electrodynamic behaviors induced by the asymmetric configurations of the magnetically coupled nonlinear energy harvesting system. Asymmetric profiles of potential energy for beam 2 are achieved by changing the offset distance between magnets 2 and 3, while all other spacing parameters remain the same as in the symmetric case. Figure 8(a) and (b) shows the asymmetric beam 2 potential energy profiles and the corresponding stable equilibria when the
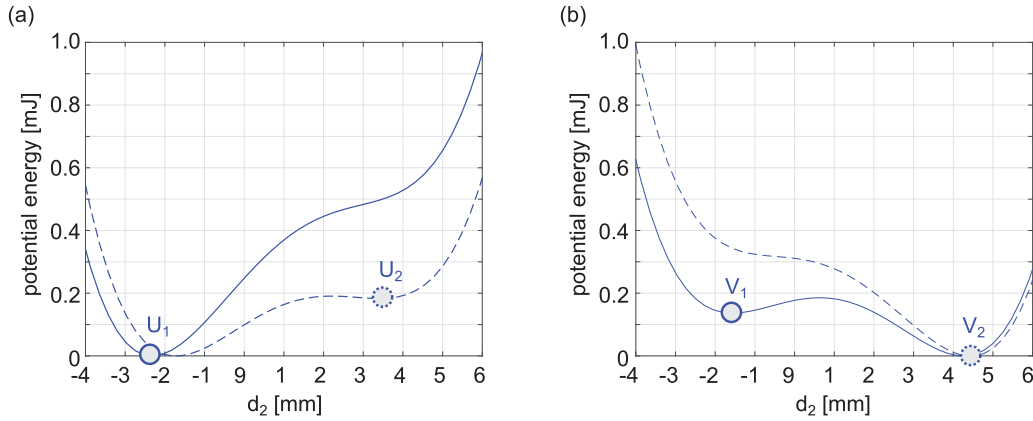
**Figure 8.** Potential energy profiles of the harvester beam 2 with magnet center offset distance between magnets 2 and 3 of (a) $\Delta_2 = -1.3$ mm and (b) $\Delta_2 = -1.05$ mm.
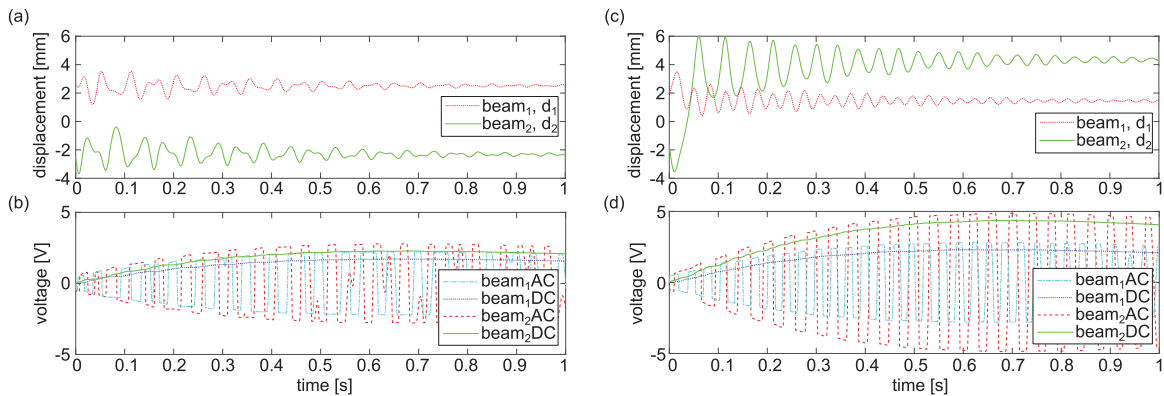


**Figure 9.** Simulation results of time series responses with an initial velocity on beam 2 of 0.25 m/s: (a, b) magnet center offset distance between magnets 2 and 3 is $\Delta_2 = -1.3$ mm, and beam 2 initially rests at stable equilibrium $U_1$; (c, d) magnet center offset distance between magnets 2 and 3 is $\Delta_2 = -1.05$ mm, and beam 2 initially rests at stable equilibrium $V_1$.

magnet center offset distance between magnets 2 and 3 are $\Delta_2 = -1.3$ mm and $\Delta_2 = -1.05$ mm, respectively. The corresponding potential energy profiles for beam 1 are not found to be greatly influenced by these small offset parametric deviations, so the potential energy profiles for beam 1 are not shown for the sake of brevity. The solid and dashed potential energy profiles in Figure 8 are evaluated in accordance with the respective pairs of beam 1 stable equilibria.

It can be seen from Figure 8(a) that when $\Delta_2 = -1.3$ mm, the beam 2 tip magnet has stable equilibria at $d_2 = -2.325$ mm ($U_1$) and $d_2 = 3.417$ mm ($U_2$). The potential energy for the stable equilibrium $U_1$ is 0.183 mJ less than the energy at stable equilibrium $U_2$. On the other hand, It can be seen from Figure 8(b) that when $\Delta_2 = -1.05$ mm, the beam 2 tip magnet has stable equilibria at $d_2 = -1.567$ mm ($V_1$) and $d_2 = 4.443$ mm ($V_2$). The potential energy of beam 2 at stable equilibrium $V_1$ is 0.136 mJ greater than that at stable equilibrium $V_2$. As exemplified in Figure 8, the minor parametric deviations on the offset distances give

rise to large asymmetries between the relative potential energies of the two stable equilibria for beam 2. For the case of $\Delta_2 = -1.3$ mm, the global minimum of potential energy is at $U_1$, whereas for $\Delta_2 = -1.05$ mm the global minimum is at $V_2$. This suggests that the basins of attraction for $U_1$ and $V_2$ are, respectively, greater than those for the alternate metastable states $U_2$ and $V_1$ (Kozinsky et al., 2007).

Using the two distinct asymmetric setups as shown in Figure 8, simulations are conducted to investigate the nonlinear impulse responses of the magnetically coupled nonlinear energy harvesting system. The results shown in Figure 9(a) and (b) and Figure 10(a) and (b) correspond to the asymmetric system configuration with beam 2 potential energy profiles shown in Figure 8(a) such that a bias exists to the stable equilibrium with a negative value of $d_2$. The results in Figures 9(c) and (d) and 10(c) and (d) correspond to the other asymmetric setup according to the beam 2 potential energy profiles in Figure 8(b), which introduces a bias toward the stable equilibrium with a positive value of $d_2$. The
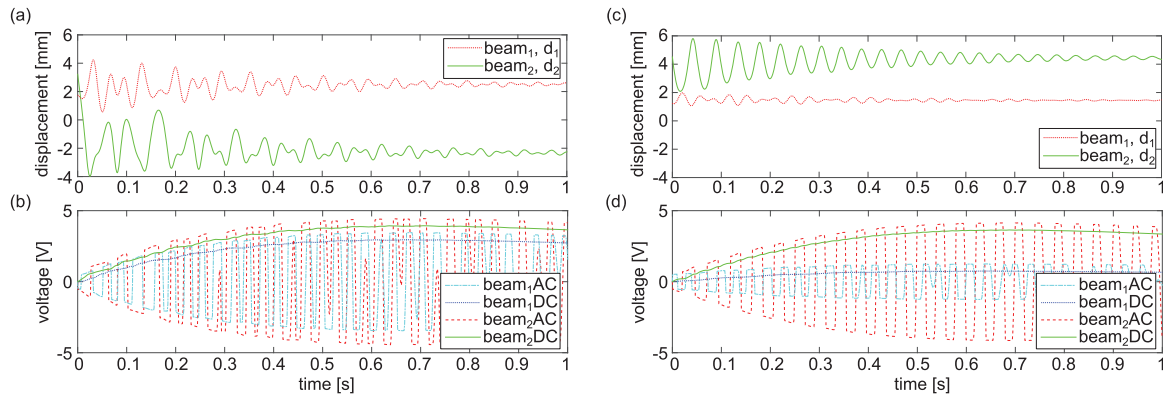
**Figure 10.** Simulation results of time series responses with an initial velocity on beam 2 of 0.25 m/s: (a, b) magnet center offset distance between magnets 2 and 3 is $\Delta_2 = -1.3$ mm, and beam 2 initially rests at stable equilibrium $U_2$; (c, d) magnet center offset distance between magnets 2 and 3 is $\Delta_2 = -1.05$ mm, and beam 2 initially rests at stable equilibrium $V_2$.

initial velocity applied to beam 2 is 0.25 m/s throughout the simulations shown in Figures 9 and 10. The difference between the results in Figures 9 and 10 and individual simulations is the initial stable equilibria.

Figure 9 presents the outcomes when beam 2 is initially perturbed from stable equilibria $U_1$ or $V_1$ in which case the beam tip magnets 1 and 2 are in closer proximity. As shown in Figure 9(a) and (b), after the impulse is applied, beam 2 continues to oscillate around stable equilibrium $U_1$, which generates sufficient magnetic force fluctuations that beam 1 also vibrates with comparable displacement amplitude. Consequently, the DC voltages rise up to around 1.72 and 2.28 V from the harvester beams 1 and 2, respectively. On the other hand, for the alternate state of asymmetry, it can be observed from Figure 9(c) and (d) that the same impulse is sufficient for beam 2 to jump from stable equilibrium $V_1$ to $V_2$. A long transient ringdown response then occurs around stable equilibrium $V_2$ for beam 2. Due to the snap-through dynamic exhibited by beam 2, beams 1 and 2 are farther away. Yet, there is still adequate magnetic force coupling before beam 2 snaps through to cause beam 1 to vibrate with notable displacement amplitude. The induced DC voltages from the harvester beams 1 and 2 are up to 2.30 and 4.37 V, respectively. The 0.136-mJ potential energy difference for beam 2 between stable equilibria $V_1$ and $V_2$ shown in Figure 8(b) helps explain, in part, the difference in overall DC voltage outputs shown in Figure 9(b) and (d).

With the same impulse of initial velocity on beam 2, Figure 10 presents the transient, nonlinear impulse response behaviors for the two asymmetric structural configurations when beam 2 initially rests at either $U_2$ or $V_2$ in which case the harvester beam tip magnets 1 and 2 are more distant from each other. It is demonstrated from Figure 10(a) and (b) that the impulse is sufficient for beam 2 to snap through from the stable equilibrium $U_2$ to $U_1$, and finally to oscillate around $U_1$

that is closer in proximity to beam 1. The nearness of the harvester beam tip mass magnets induces considerable magnetic force coupling and thus energetic AC voltage generation. The resulting DC voltages increase up to around 2.96 and 3.94 V, respectively, for harvester beams 1 and 2 as shown in Figure 10(b). Comparatively, from Figure 10(c) and (d) it can be seen that such impulse induces vibrations of beam 2 around the stable equilibrium $V_2$. Weaker magnetic force coupling is thus created between the harvester beams and beam 1 experiences insignificant oscillations. Although the DC voltage from harvester beam 2 is nearly 3.64 V in this case, the DC voltage from beam 1 is just 0.75 V. Here the enhanced DC voltage generation can likewise be partly explained by the potential energy release that beam 2 experiences in transitioning from a resting state of $U_2$ to a final resting state of $U_1$ which occurs in the results of Figure 10(b) but not in the example of Figure 10(d).

A quantitative contrast may be made to emphasize the unique magnetic force coupling manifest in the asymmetric configurations of the energy harvesting system. From Figures 9(b) and 10(b), the ratios of maximum DC voltage outputs between the harvester beams 1 and 2 are 0.754 and 0.751, respectively. This asymmetric configuration exhibits a global minimum of potential energy for beam 2 such that it comes to rest with negative values of $d_2$, which are nearer to harvester beam 1 and its tip magnet. Thus, this asymmetric configuration yields consistent ratios of the DC voltages due to a more influential force coupling between the harvester beams via the corresponding tip magnets. This contrasts with the asymmetric system configuration studied in Figures 9(d) and 10(d) whereby the global minimum of potential energy for beam 2 is such that that beam comes to rest with positive values of $d_2$. In this case, the results in Figures 9(d) and 10(d) show that the ratios of maximum DC voltage outputs between the harvester beams 1 and 2 are 0.526 and
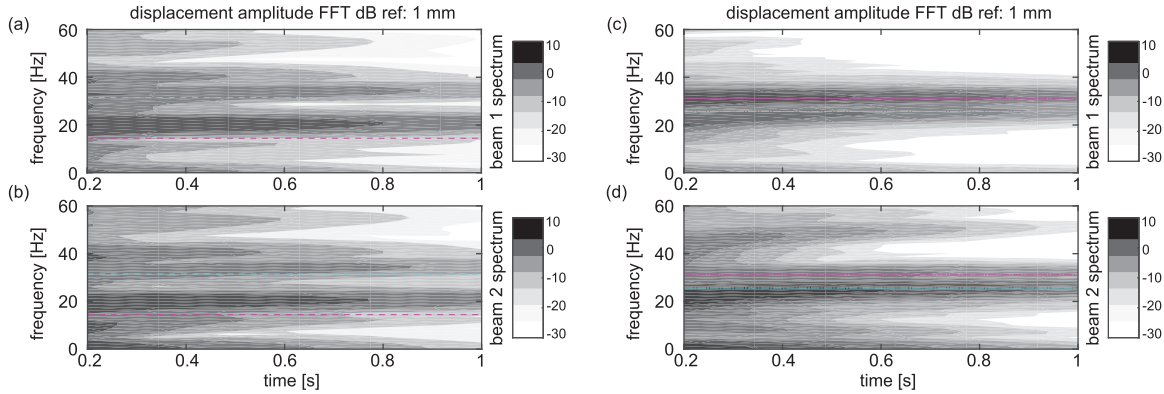
**Figure 11.** Simulation results of time–frequency distributions corresponding to (a, b) time series displacement in Figure 10(a), and (c, d) time series displacement in Figure 9(c).

0.206, respectively. Thus, the relative nearness of the stable equilibrium positions for beams 1 and 2 is strongly correlated to the relative impulsive energy transfer achieved due to the noncontact magnetic force coupling in the system.

The frequency response of these nonlinear impulse responses sheds further light on the coupling influences and the resulting charging power generation. To establish a baseline of relevant natural frequencies of free oscillation, the equation (10) for the magnetic forces is linearized using Taylor series expansions around statically stable equilibria

$$F_{21} \approx \beta_{21,1} x_1 + \beta_{21,2} x_2 \qquad (13a)$$

$$F_{31} \approx \beta_{31,1} x_1 \qquad (13b)$$

$$F_{12} \approx \beta_{12,1} x_1 + \beta_{12,2} x_2 \qquad (13c)$$

$$F_{32} \approx \beta_{32,2} x_2 \qquad (13d)$$

where $\beta_{mn,i}$ ($i = 1, 2$) denote the coefficients provided in Appendix 1 that relate the magnetic force acting on magnet $n$ due to the effects of magnet $m$ along the transverse direction of either $\hat{i}$ or $\hat{j}$ as indicated in Figure 2.

The undamped eigenvalue problem for the magnetically coupled energy harvesting system is then composed from the governing equations

$$\begin{bmatrix} m_1 & 0 \\ 0 & m_2 \end{bmatrix} \begin{bmatrix} \ddot{x}_1 \\ \ddot{x}_2 \end{bmatrix} + \begin{bmatrix} k_{11} - \beta_{21,1} - \beta_{31,1} & -\beta_{21,2} \\ -\beta_{12,1} & k_{12} - \beta_{12,2} - \beta_{32,2} \end{bmatrix}$$
$$\begin{bmatrix} x_1 \\ x_2 \end{bmatrix} = \begin{bmatrix} 0 \\ 0 \end{bmatrix}$$
$$(14)$$

that yield the frequency equation

$$(m_1 \lambda^2 + k_{11} - \beta_{21,1} - \beta_{31,1})$$
$$(m_2 \lambda^2 + k_{12} - \beta_{12,2} - \beta_{32,2}) \qquad (15)$$
$$- \beta_{21,2} \beta_{12,1} = 0$$

Based on the statically stable equilibria around which oscillations occur, different eigenvalues $\lambda$ and hence natural frequencies are computed from equation (15). These may be contrasted to the instantaneous frequency response of the nonlinear impulsive vibrations.

Figure 11 presents the short-time fast Fourier transform (SFFT) of the time series of harvester beam displacements. The results from Figure 11(a) and (b) correspond to the beam displacement spectra in dB using the time series shown in Figure 10(a). The spectra in Figure 11(c) and (d) correspond to the time series displacement in Figure 9(c).

Based on the frequency response shown in Figure 11(a) and (b), the harvester beams share primary spectral characteristics. In particular, both beams have notable peaks in the transient frequency response around 20 and 34 Hz. The spectral peaks in Figure 11(a) and (b) are near, but not identical, to the corresponding natural frequencies 14.5 and 31.5 Hz, denoted by dashed lines. For both harvester beams, the spectral peak of displacement around 20 Hz is about 7 dB greater than that for the response around 34 Hz. In addition, Figure 11(a) and (b) reveals notable spectral peaks around the second-order harmonic of 40 Hz. These results provide evidence that, for this asymmetric configuration of the energy harvesting system, a strong magnetic coupling effect exists between the harvester beams, such that the primary frequencies of oscillation in the nonlinear impulsive vibrations are not identical to the linearized natural frequencies of the system configuration.

The time–frequency distributions in Figure 11(c) and (d) correspond to the case that the harvester beams vibrate with the impulse response shown in Figure 9(c). As shown in Figure 11(c), the oscillation of beam 1 has a major spectral peak around 31.2 Hz and another peak near 25 Hz that is about 6 dB smaller in amplitude. As shown in Figure 11(d), beam 2 exhibits primary frequencies of transient oscillation near 25 Hz that is around 10 dB greater in amplitude than the
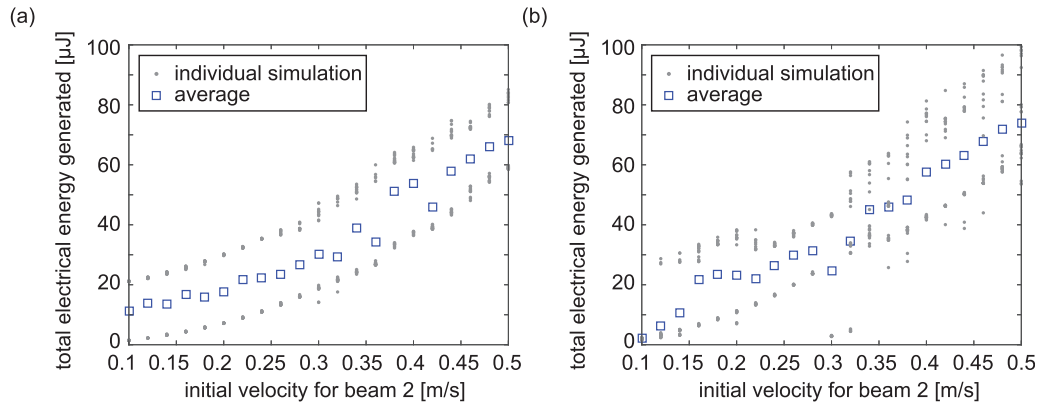
**Figure 12.** Individual simulations (dots) and averaged values (squares) of total electrical energy generated by the energy harvesting system. Results in (a) correspond to the asymmetric potential energy profile for beam 2 shown in Figure 8(a), while results in (b) correspond to the profile shown in Figure 8(b).

peak near 31.2 Hz and the second harmonic peak around 50 Hz. These primary spectral peaks for beams 1 and 2 are close in frequency to the linearized natural frequencies of 25.62 and 31.16 Hz computed by equation (15) and shown by dot-dashed lines in Figure 11(c) and (d). Because the primary spectral responses of the beams are indeed close to the linearized natural frequencies, the asymmetric configuration of the energy harvesting system, such that the global minimum of potential energy for beam 2 is further distant from beam 1, results in less substantial magnetic coupling between the harvester beams. This explains why the harvester beams 1 and 2 primarily oscillate at the linearized natural frequencies.

Considering these results in tandem with observations of the DC powers delivered by each asymmetric setup of the energy harvesting system, it is found that the greater magnetic coupling between the harvester beams increases the DC voltage output.

### Energy conversion capability evaluation

Based on the nonlinear impulse responses featured in Figures 9 and 10, the rectified voltages are strongly dependent upon the initial stable equilibria from which the impulsive perturbation injects energy into beam 2. As demonstrated by the transient responses, the magnetic force coupling effects cause distinct exchange and transfer of the impulsive energy from beam 2 to beam 1 based on these initial stable equilibria.

For greater insight on such energy conversion characteristics, simulations are conducted to study the total electrical energy generation achieved as a function of a wide range of initial impulse amplitudes, proportional to the initial velocity acting on beam 2. Figure 12 presents the total electrical energy stored on the smoothing capacitors $C_{ri}$ using dots for individual simulation results at a given initial velocity, while squares represent the corresponding averaged values of total energy

for the respective initial velocity increment. For each initial velocity, 24 random initial conditions of displacement, normally distributed around a stable equilibrium, are utilized to obtain significant statistics. The results in Figure 12(a) and (b) correspond to the cases when the beam 2 potential energy profiles are asymmetric as shown in Figure 8(a) and (b), respectively.

As observed in the results from Figure 12, two levels of total electrical energy may be generated from the nonlinear energy harvester system. Such trend is unique when compared to the system examined in the results of Figure 7(b) for which the potential energy profile of beam 2 is mirror symmetric. The distinct electrical energy quantities generated for a given initial velocity by the asymmetric energy harvesting systems represented in Figure 12(a) and (b) are due to the different initial stable equilibria from which beam 2 is perturbed. Namely, when the impulse causes beam 2 to move from a stable equilibrium of greater potential energy to a final resting position of lower potential energy, a proportion of that potential energy difference is also converted into electrical energy. This is the origin of the discrete jump in electrical energy generation shown between the individual simulation results throughout Figure 12. The discrete increase of total electrical energy is about one order of magnitude smaller than the release of beam 2 potential energy, which exemplifies the roles of inherent mechanical damping and relatively low electromechanical coupling on diminishing the direct and total conversion of the potential energy release.

To contrast these results with asymmetric configurations of the system to the mirror symmetric counterpart, the average electrical energy generations from each of beam 1 and beam 2 are shown in Figure 13. The portions of electrical energy contributed from beam 1 are presented by bars of dark shading, while the contributions from beam 2 are shown by bars of light shading. Each portion of shaded bar at a given
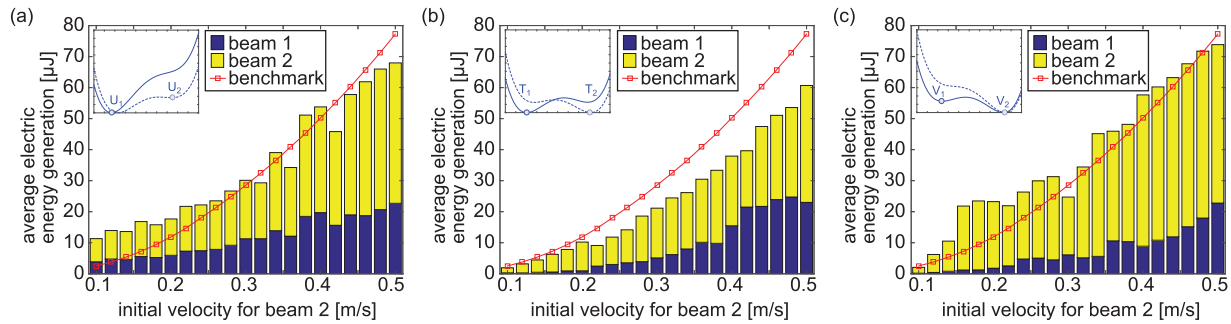
**Figure 13.** Total electrical energy generated from beam 1 (dark blue shaded bars) and beam 2 (light yellow shaded bars): (a) results shown for asymmetric system configuration corresponding to potential energy profile in Figure 8(a); (b) results shown for mirror symmetric system configuration corresponding to potential energy profile in Figure 4(b); (c) results shown for asymmetric system configuration corresponding to potential energy profile in Figure 8(b); total electrical energy generated from the benchmark, single nonlinear harvester, which is shown by red solid curve with square marker.

initial velocity is the mean of the 24 simulation cases presented in Figure 12. The sum of the bar heights denotes the total electrical energy generated for a given initial velocity. To strictly quantify the roles of the non-contact magnetic coupling on promoting enhanced energy capture and conversion in the system investigated here, Figure 13 also shows the results by the solid curve with square markers for a benchmark energy harvester. The benchmark is a single nonlinear energy harvester equivalent to the piezoelectric "beam 2" on its own with the repulsive magnetic force action provided by a reference-grounded magnet, like magnet 3 in the present system configuration. The benchmark harvester is tuned such that the two stable equilibria and the potential energy barrier are identical to those achieved for beam 2 for the mirror symmetric case shown in Figure 4(b).

Results in Figure 13 consider a resistance $R_i = 1000$ k$\Omega$ ($i = 1, 2$). Figure 14 complements this comparison by quantifying the kinetic-to-electrical energy conversion efficiency as functions of load resistance $R_i$ ($i = 1, 2$). This efficiency measure is the ratio of total electrical energy generated to the initial kinetic energy on beam 2 due to an impulse of 0.25 m/s initial velocity. To study the influence of the initial stable equilibrium condition for the energy harvesting system, the green circles and blue filled data points in Figure 14, respectively, indicate that the beam 2 initial displacement condition is closer to or farther away from the beam 1 resting position. The energy conversion efficiency of the benchmark, single nonlinear energy harvester is presented by the red solid curve with square markers.

When beam 2 adopts the mirror symmetric potential energy profile, it is revealed from Figure 13(b) that the total electrical energy generated by the system is approximately the same as that created by the benchmark when the initial velocities are less than around 0.2 m/s. Interestingly, this also corresponds to transient responses for which the dynamic contributions from beam 1 are negligible since the dark shaded bars in Figure 13(b) have insignificant contribution for initial velocities less than around 0.2 m/s. Yet, when initial velocities acting on beam 2 exceed 0.2 m/s, a greater transfer of impulsive energy to beam 1 is achieved and the proportion of total electrical energy generated by the system provided by beam 1 increases. Simultaneously, this mirror symmetric configuration of the energy harvesting system is less effective than the single nonlinear energy harvester benchmark, seen by the greater disparity between the total energy levels in Figure 13(b) for initial velocities above 0.2 m/s. These observations are supported by the contrast in Figure 14(b). The energy conversion efficiency of the mirror symmetric configuration of the magnetically coupled energy harvesting system is always less than that of the benchmark harvester regardless of load resistance selection. These results provide evidence that the magnetic coupling effects in the nonlinear energy harvesting system can reduce the total electrical energy compared to the single harvester benchmark if the system configuration is tuned to adopt a near-mirror-symmetric potential energy profile for beam 2.

Asymmetry in the system is found to greatly change the situation and introduce favorable energy conversion opportunity. As shown in Figure 13(a), the total electrical energy from the magnetically coupled nonlinear energy harvesting system clearly exceeds the energy generated by the benchmark nonlinear energy harvester when the initial velocities are less than around 0.25 m/s. According to the corresponding energy conversion efficiency results in Figure 14(a), for this asymmetric case when beam 2 possesses a bias to come to rest nearer to beam 1 the energy conversion efficiency may be as great as 17.5% or as little as 5.8% if the optimal resistance is selected. The mean of these efficiency values (11.6%) is still greater than that of the benchmark harvester that delivers 9.8% conversion efficiency at its
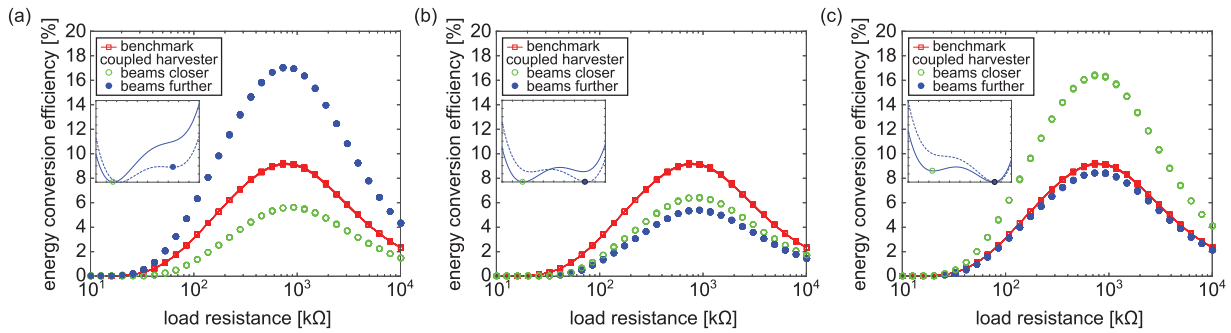
**Figure 14.** Kinetic-to-electrical energy conversion efficiency when beam 2 is perturbed from the stable equilibrium closer to beam 1 (green circle) or from the stable equilibrium farther away from beam 1 (blue filled points) with an initial velocity of 0.25 m/s: (a) results shown for asymmetric system configuration corresponding to potential energy profile in Figure 8(a); (b) results shown for mirror symmetric system configuration corresponding to potential energy profile in Figure 4(b); (c) results shown for asymmetric system configuration corresponding to potential energy profile in Figure 8(b); corresponding results for the benchmark, single nonlinear harvester, which are shown by a red solid curve with square marker.

best. In other words, given a large number of initial displacement conditions, the asymmetric system with the potential energy bias having beam 2 positioned nearer to beam 1 is more efficient on the mean in the kinetic-to-electrical energy conversion process than the benchmark, as long as the initial velocity is not too large. In fact, a similar conclusion is drawn according to the statistics obtained for the other asymmetric case when beam 2 has a global minimum of potential energy at the stable equilibrium $V_2$. From Figure 13(c), when the initial velocity acting on beam 2 is less than around 0.3 m/s, the nonlinear energy harvesting system with magnetic coupling exceeds the total energy created by the benchmark harvester. Above this initial velocity range, the total electrical energy generated by the system is approximately the same as the benchmark. It can be seen from Figure 14(c) that for this asymmetric case when beam 2 is likely to come to rest with deflections farther away from beam 1, the energy conversion efficiency may be as great as 16.4% or as little as 8.4% if the optimal resistance is selected. The mean efficiency of 12.4% is likewise greater than the maximum efficiency of the benchmark harvester, that is, 9.8%. It is observed that the optimal values of load resistance as shown in Figure 14 are all around the same level, which agrees with the findings of a prior report that nonlinearity types do not influence the selection of optimal load resistance in AC–DC rectifiers (Dai and Harne, 2018). These results emphasize opportunities and potential challenges due to initial condition sensitivities of using asymmetric setups to improve magnetically coupled nonlinear energy harvester performance under impulsive excitations.

Because the asymmetric versions of the magnetically coupled energy harvesting system both deliver greater DC power than the more mirror symmetric counterpart system on the mean for relatively small initial velocities,

it becomes necessary to differentiate the energy conversion capabilities between the two versions of asymmetry that may be exploited. As shown in Figure 13(a) and (c), the relative ratios of contributions from harvester beam 2 and beam 1 to the total electrical energy are significantly different for the two asymmetric cases. When beam 2 has a global minimum of potential energy toward stable equilibrium $U_1$, it is observed from Figure 13(a) that the ratio of contributions from harvester beam 2 and beam 1 to the total electrical energy is around 7/4, which is consistent across a large range of initial velocities acting on beam 2. On the other hand, when beam 2 has a global minimum of potential energy at the stable equilibrium $V_2$, as shown in Figure 13(c) over a wide range of initial velocities the greatest proportion of electrical energy contribution is consistently provided by beam 2. The ratio of electrical energy delivered from the harvester beam 2 to beam 1 is around 3/1 or greater in this case.

These results emphasize the discoveries of this work that strong magnetic force coupling is directly influential on the electrical energy delivery from the energy harvesting system. The interpretations of these influences are captured by a practical example. When the electrical energy contributions are unequal between the harvester beams, such as for the asymmetric configuration characterized in Figure 13(c), a greater detriment to the overall system performance would be encountered should electrical failure occur for beam 2. Yet, the asymmetric harvesting system given by a global stable equilibrium for beam nearer to beam 1 (Figure 13(a)) would not have as severe performance loss should electrical failure come to beam 2. On the other hand, one could easily exploit the imbalance of electrical energy generation between the harvester beams shown in Figure 13(c) and use a more electromechanically coupled material for beam 2, such as PMN-PT,

since harvester beam 2 delivers the greater proportion of electrical energy. Thus, robustness and performance issues help interpret the contrast between the different asymmetric configurations of the magnetically coupled nonlinear energy harvesting system.

## Conclusion

To characterize the nonlinear coupling and energy conversion properties of a magnetically coupled energy harvesting system, this research investigates the dynamic response of a multi-directional energy harvesting system subjected to impulsive energy inputs. A model of the system is composed and validated by experimentation on a counterpart proof-of-concept platform. Taking advantage of the model, the intricate dynamic behaviors of the magnetically coupled harvester system are scrutinized according to the influence of different potential energy profiles tuned via the magnetic force coupling. When subjected to a broad range of impulsive excitations, total electrical energy generation and energy conversion efficiency are clearly dependent upon the presence and type of asymmetry that is manifest in the system. Symmetric configurations of the system are discovered to be detrimental to kinetic-to-electrical energy conversion, when compared to an individual nonlinear energy harvester, whereas asymmetry may magnify the absolute energy capture and efficiency of conversion. On the other hand, asymmetric configurations may also release stored elastic energy that is not manifest in symmetric systems. The selection of a type of asymmetry, whether with bias of the harvester beams toward or away from each other in the global stable equilibrium, may be made based on practical considerations of the system composition and deployment. The results of this research provide insights about potential opportunities and challenges to incorporate magnetic coupling effects in nonlinear energy harvesting systems subjected to impulsive energies.

### Declaration of conflicting interests

The author(s) declared no potential conflicts of interest with respect to the research, authorship, and/or publication of this article.

### Funding

### ORCID iD

Ryan L Harne https://orcid.org/0000-0003-3124-9258

## References

Andò B, Baglio S, Maiorca F, et al. (2013) Analysis of two dimensional, wide-band, bistable vibration energy harvester. *Sensors and Actuators A: Physical* 202: 176–182.

Ansari MH and Karami MA (2015) Energy harvesting from controlled buckling of piezoelectric beams. *Smart Materials and Structures* 24: 115005.

Dai Q and Harne RL (2018) Charging power optimization for nonlinear vibration energy harvesting systems subjected to arbitrary, persistent base excitations. *Smart Materials and Structures* 27: 015011.

Erturk A (2011) Piezoelectric energy harvesting for civil infrastructure system applications: moving loads and surface strain fluctuations. *Journal of Intelligent Material Systems and Structures* 22: 1959–1973.

Erturk A and Inman DJ (2009) An experimentally validated bimorph cantilever model for piezoelectric energy harvesting from base excitations. *Smart Materials and Structures* 18: 025009.

Erturk A and Inman DJ (2011) Broadband piezoelectric power generation on high-energy orbits of the bistable Duffing oscillator with electromechanical coupling. *Journal of Sound and Vibration* 330: 2339–2353.

Erturk A, Hoffmann J and Inman DJ (2009) A piezomagnetoelastic structure for broadband vibration energy harvesting. *Applied Physics Letters* 94: 254102.

Feeny BF and Yuan CM (2001) Parametric identification of an experimental magneto-elastic oscillator. *Journal of Sound and Vibration* 247: 785–806.

Gu L and Livermore C (2011) Impact-driven, frequency up-converting coupled vibration energy harvesting device for low frequency operation. *Smart Materials and Structures* 20: 045004.

Guyomar D, Badel A, Lefeuvre E, et al. (2005) Toward energy harvesting using active materials and conversion improvement by nonlinear processing. *IEEE Transactions on Ultrasonics, Ferroelectrics, and Frequency Control* 52: 584–595.

Harne RL and Wang KW (2014) Prospects for nonlinear energy harvesting systems designed near the elastic stability limit when driven by colored noise. *Journal of Vibration and Acoustics* 136: 021009.

Harne RL and Wang KW (2017) *Harnessing Bistable Structural Dynamics: For Vibration Control, Energy Harvesting and Sensing*. Chichester: John Wiley & Sons.

Harne RL, Zhang C, Li B, et al. (2016) An analytical approach for predicting the energy capture and conversion by impulsively-excited bistable vibration energy harvesters. *Journal of Sound and Vibration* 373: 205–222.

Hikihara T and Kawagoshi T (1996) An experimental study on stabilization of unstable periodic motion in magneto-elastic chaos. *Physics Letters A* 211: 29–36.

Hodges DH (1984) Proper definition of curvature in nonlinear beam kinematics. *AIAA Journal* 22: 1825–1827.

Jung SM and Yun KS (2010) Energy-harvesting device with mechanical frequency-up conversion for increased power efficiency and wideband operation. *Applied Physics Letters* 96: 111906.

Kozinsky I, Postma HWC, Kogan O, et al. (2007) Basins of attraction of a nonlinear nanomechanical resonator. *Physical Review Letters* 99: 207201.

Kulah H and Najafi K (2008) Energy scavenging from low-frequency vibrations by using frequency up-conversion for wireless sensor applications. *IEEE Sensors Journal* 8: 261–268.

Lin Z, Chen J, Li X, et al. (2016) Broadband and three-dimensional vibration energy harvesting by a non-linear magnetoelectric generator. *Applied Physics Letters* 109: 253903.

Masana R and Daqaq MF (2011) Relative performance of a vibratory energy harvester in mono- and bi-stable potentials. *Journal of Sound and Vibration* 330: 6036–6052.

Moon FC and Holmes PJ (1979) A magnetoelastic strange attractor. *Journal of Sound and Vibration* 65: 275–296.

Panyam M, Masana R and Daqaq MF (2014) On approximating the effective bandwidth of bi-stable energy harvesters. *International Journal of Non-Linear Mechanics* 67: 153–163.

Pillatsch P, Yeatman EM and Holmes AS (2012) A scalable piezoelectric impulse-excited energy harvester for human body excitation. *Smart Materials and Structures* 21: 115018.

Randall RB (2011) *Vibration-Based Condition Monitoring: Industrial, Aerospace and Automotive Applications*. Chichester: John Wiley & Sons.

Roundy S, Wright PK and Rabaey J (2003) A study of low level vibrations as a power source for wireless sensor nodes. *Computer Communications* 26: 1131–1144.

Schaeffer M and Ruzzene M (2015) Wave propagation in multistable magneto-elastic lattices. *International Journal of Solids and Structures* 56–57: 78–95.

Scruggs J and Jacob P (2009) Harvesting ocean wave energy. *Science* 323: 1176–1178.

Seuaciuc-Osório T and Daqaq MF (2010) Energy harvesting under excitations of time-varying frequency. *Journal of Sound and Vibration* 329: 2497–2515.

Shenck NS and Paradiso JA (2001) Energy scavenging with shoe-mounted piezoelectrics. *IEEE Micro* 21: 30–42.

Shu YC and Lien IC (2006) Analysis of power output for piezoelectric energy harvesting systems. *Smart Materials and Structures* 15: 1499–1512.

Simitses GJ (1990) *Dynamic Stability of Suddenly Loaded Structures*. New York: Springer.

Stacoff A, Diezi C, Luder G, et al. (2005) Ground reaction forces on stairs: effects of stair inclination and age. *Gait and Posture* 21: 24–38.

Stanton SC, McGehee CC and Mann BP (2010) Nonlinear dynamics for broadband energy harvesting: investigation of a bistable piezoelectric inertial generator. *Physica D* 239: 640–653.

Su WJ and Zu JW (2013) An innovative tri-directional broadband piezoelectric energy harvester. *Applied Physics Letters* 103: 203901.

Su WJ and Zu JW (2014) Design and development of a novel bi-directional piezoelectric energy harvester. *Smart Materials and Structures* 23: 095012.

Suhaimi K, Ramlan R and Putra A (2014) A combined softening and hardening mechanism for low frequency human motion energy harvesting application. *Advances in Acoustics and Vibration* 2014: 217032.

Tang L, Yang Y and Soh CK (2010) Toward broadband vibration-based energy harvesting. *Journal of Intelligent Material Systems and Structures* 21: 1867–1897.

Umeda M, Nakamura K and Ueha S (1996) Analysis of the transformation of mechanical impact energy to electric energy using piezoelectric vibrator. *Japanese Journal of Applied Physics* 35: 3267.

Virgin LN and Wiebe R (2013) On damping in the vicinity of critical points. *Philosophical Transactions of the Royal Society A* 371: 20120426.

Wickenheiser AM and Garcia E (2010) Broadband vibration-based energy harvesting improvement through frequency up-conversion by magnetic excitation. *Smart Materials and Structures* 19: 065020.

Yang J, Wen Y, Li P, et al. (2013) A two-dimensional broadband vibration energy harvester using magnetoelectric transducer. *Applied Physics Letters* 103: 243903.

Yang W and Towfighian S (2017a) A hybrid nonlinear vibration energy harvester. *Mechanical Systems and Signal Processing* 90: 317–333.

Yang W and Towfighian S (2017b) Internal resonance and low frequency vibration energy harvesting. *Smart Materials and Structures* 26: 095008.

Ylli K, Hoffmann D, Willmann A, et al. (2015) Energy harvesting from human motion: exploiting swing and shock excitations. *Smart Materials and Structures* 24: 025029.

Yung KW, Landecker PB and Villani DD (1998) An analytic solution for the force between two magnetic dipoles. *Physical Separation in Science and Engineering* 9: 39–52.

Zhang Y, Leng Y and Fan S (2017) The accurate analysis of magnetic force of bi-stable piezoelectric cantilever energy harvester. In: *ASME 2017 international design engineering technical conferences and computers and information in engineering conference*, Cleveland, OH, 6–9 August 2017, paper no. DETC2017-67168.

# Appendix I

## Coefficients of linearized magnetic forces

The constant coefficients of simplified magnetic forces as shown in equation (13) are calculated by Mathematica, using Taylor series expansion. All the magnetic forces are linearized around the stable equilibria denoted by $(x_{s1}, x_{s2})$

$$\beta_{21,1} = \frac{3M_1M_2V_1V_2\left(3L^4 - 24L^2x_{s1}^2 + 8x_{s1}^4 + 12L^3x_{s2} - 48Lx_{s1}^2x_{s2} + 18L^2x_{s2}^2 - 24x_{s1}^2x_{s2}^2 + 12Lx_{s2}^3 + 3x_{s2}^4\right)\mu}{4\pi\left(L^2 + x_{s1}^2 + 2Lx_{s2} + x_{s2}^2\right)^{9/2}} \tag{16a}$$

$$\beta_{21,2} = \frac{15M_1M_2V_1V_2x_{s1}(L + x_{s2})\left(-3L^2 + 4x_{s1}^2 - 6Lx_{s2} - 3x_{s2}^2\right)\mu}{4\pi\left(L^2 + x_{s1}^2 + 2Lx_{s2} + x_{s2}^2\right)^{9/2}} \tag{16b}$$

$$\beta_{31,1} = \frac{-3M_1M_3V_1V_3\left(8H^4 - 24H^2L^2 + 3L^4 - 32H^3x_{s1} + 48HL^2x_{s1} + 48H^2x_{s1}^2 - 24L^2x_{s1}^2 - 32Hx_{s1}^3 + 8x_{s1}^4\right)\mu}{4\pi\left(H^2 + L^2 - 2Hx_{s1} + x_{s1}^2\right)^{9/2}} \tag{16c}$$

$$\beta_{12,1} = \frac{15M_1M_2V_1V_2x_{s1}(L + x_{s2})\left(-3L^2 + 4x_{s1}^2 - 6Lx_{s2} - 3x_{s2}^2\right)\mu}{4\pi\left(L^2 + x_{s1}^2 + 2Lx_{s2} + x_{s2}^2\right)^{9/2}} \tag{16d}$$

$$\beta_{12,2} = \frac{-3M_1M_2V_1V_2\left(4L^4 - 27L^2x_{s1}^2 + 4x_{s1}^4 + 16L^3x_{s2} - 54Lx_{s1}^2x_{s2} + 24L^2x_{s2}^2 - 27x_{s1}^2x_{s2}^2 + 16Lx_{s2}^3 + 4x_{s2}^4\right)\mu}{4\pi\left(L^2 + x_{s1}^2 + 2Lx_{s2} + x_{s2}^2\right)^{9/2}} \tag{16e}$$

$$\beta_{32,2} = \frac{3M_2M_3V_2V_3\left(4H^4 - 27H^2x_{s2}^2 + 4x_{s2}^4\right)\mu}{4\pi\left(H^2 + x_{s2}^2\right)^{9/2}} \tag{16f}$$